

ERIS: An Energy-Guided Feature Disentanglement Framework for Out-of-Distribution Time Series Classification

Xin Wu¹, Fei Teng^{1,2*}, Ji Zhang¹, Xingwang Li¹, Yuxuan Liang³

¹School of Computing and Artificial Intelligence, Southwest Jiaotong University, Chengdu, China

²Engineering Research Center of Sustainable Urban Intelligent Transportation, Ministry of Education, Chengdu, China

³The Hong Kong University of Science and Technology (Guangzhou), Guangzhou, China

{xinwu, lixingwang}@my.swjtu.edu.cn; {fteng,jizhang}@swjtu.edu.cn; yuxliang@outlook.com

Abstract

An ideal time series classification (TSC) should be able to capture invariant representations, but achieving reliable performance on out-of-distribution (OOD) data remains a core obstacle. This obstacle arises from the way models inherently entangle domain-specific and label-relevant features, resulting in spurious correlations. While feature disentanglement aims to solve this, current methods are largely unguided, lacking the semantic direction required to isolate truly universal features. To address this, we propose an end-to-end **Energy-Regularized Information for Shift-Robustness (ERIS)** framework to enable guided and reliable feature disentanglement. The core idea is that effective disentanglement requires not only mathematical constraints but also semantic guidance to anchor the separation process. ERIS incorporates three key mechanisms to achieve this goal. Specifically, we first introduce an energy-guided calibration mechanism, which provides crucial semantic guidance for the separation, enabling the model to self-calibrate. Additionally, a weight-level orthogonality strategy enforces structural independence between domain-specific and label-relevant features, thereby mitigating their interference. Moreover, an auxiliary adversarial training mechanism enhances robustness by injecting structured perturbations. Experiments demonstrate that ERIS improves upon state-of-the-art baselines by an average of 4.04% accuracy across four benchmarks.

Introduction

Imagine an AI that flawlessly classifies life-threatening cardiac arrhythmias from ECG signals in one hospital, but is dangerously unreliable in the emergency room next door. This is not a hypothetical scenario; it is the reality of the out-of-distribution (OOD) problem (Hendrycks et al. 2021). This challenge poses a direct threat to the reliability of time series classification (TSC), a cornerstone technology now vital across a broad range of scientific and industrial fields (Gupta et al. 2020; Shi et al. 2024).

The threat of OOD failure is a well-known limitation, but this challenge is particularly severe in time series. Unlike computer vision, where style (e.g., cartoon) and content (e.g., cat) are often spatially separable, time series deeply entangles domain-specific biases (e.g., sensor calibrations) with label-relevant features (e.g., health conditions) (Kaur

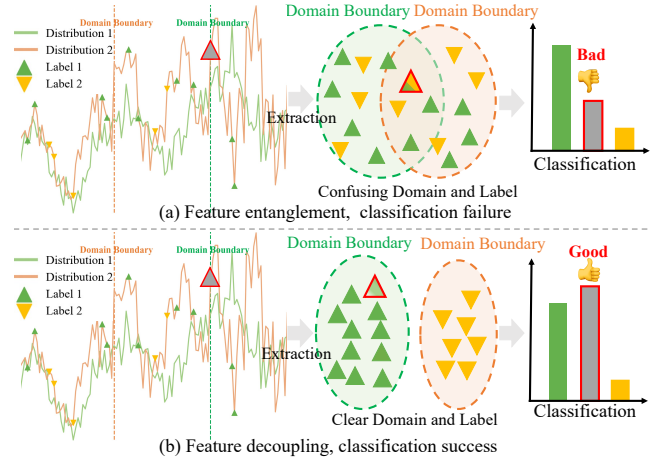


Figure 1: Illustration of domain and label decoupling impact on classification. (a) Coupled features lead to entangled representations, causing poor label separation and reduced accuracy. (b) Decoupled features enable invariant representations, improving label separation and performance.

et al. 2023; Lu et al. 2024). This temporal and nonlinear entanglement prevents models from learning truly domain-agnostic features, resulting in ambiguous decision boundaries and unreliable performance when faced with data from new or unseen environments (Jian, Yang, and Jiao 2024).

To address these challenges, recent research has explored from early implicit alignment approaches to more advanced explicit disentanglement frameworks (Li et al. 2023; Gupta et al. 2025). For example, GLIE (Qian, Pan, and Miao 2021) explores disentanglement by enforcing independence among latent variables, while ITSR (Shi et al. 2024) introduces orthogonality constraints to explicitly separate features. These works have made progress in exploring the feasibility of disentanglement. However, through in-depth analysis, we identify a deeper and often overlooked issue that the separation processes in existing frameworks are largely unguided. Whether based on orthogonality or independence, these constraints offer only mathematical guidance for separation, without incorporating any semantic guidance to inform which information should be assigned to which subspace. As a result, during optimization, the model can easily

*Corresponding author.

converge to a trivial solution that satisfies the mathematical constraints but offers no meaningful OOD generalization. For instance, ITSR imposes orthogonality, but its features remain semantically entangled, forming a checkerboard pattern in the correlation matrix (see Figure 4). Conceptually, this entanglement leads to the ambiguous boundaries of Figure 1(a), in sharp contrast to the ideal, clearly disentangled clusters in Figure 1(b). This observation raises a research question of paramount importance:

How can guided disentanglement be achieved to facilitate a reliable decomposition into domain-specific and label-relevant features?

Answering this question is fundamental to achieving reliable and generalizable performance in TSC. In this work, we propose an **Energy-Regularized Information for Shift-Robustness (ERIS)** framework to enable guided and reliable feature disentanglement for TSC. The philosophy of energy-based models (EBMs) (LeCun et al. 2006) guides the design of ERIS, which circumvents the often intractable task of learning a normalized probability distribution by instead learning a direct energy function to score data compatibility. Critically for time series, the physical energy (such as spectral energy or variance) is domain-specific and closely related to the label (Li et al. 2024). The core idea of ERIS is that effective disentanglement requires not only mathematical constraints but also such semantic guidance that can anchor the separation process.

To this end, ERIS incorporates three key mechanisms. **Firstly**, an energy-guided calibration mechanism leverages this principle to directly address unguided disentanglement by learning to assign low energy to well-aligned features and high energy to poorly aligned ones. More importantly, by linking these energy scores to model uncertainty, ERIS becomes self-calibrating. When confronted with OOD samples that trigger high-energy responses, it automatically lowers confidence, thereby suppressing overconfident, incorrect predictions. **Secondly**, a weight-level orthogonality strategy is employed to enforce structural independence between domain-specific and label-relevant representations, thereby mitigating mutual interference. **Thirdly**, an auxiliary adversarial training mechanism injects structured domain perturbations into the feature space to encourage the learning of invariant, disentangled features. Compared to the most competitive state-of-the-art (SOTA) baselines, ERIS achieves an average accuracy improvement of 4.04% on four datasets.

The main contributions of this work are threefold:

- We establish that excessively entangled domain relationships undermine the model’s ability to learn invariant features.
- We propose the ERIS framework, which imposes effective weight-level orthogonality as a mathematical constraint and incorporates energy-based guidance to reliably disentangle domain-specific and label-relevant features.
- A domain-disentangled adversarial training mechanism

is designed to mitigate structured perturbations that reflect domain discrepancies during training.

Related Work

OOD in Time Series Classification

OOD generalization is a key problem in reliable AI. Existing methods fall into two main aspects. The first is robust optimization. It improves resistance to distribution shifts by minimizing worst-case risk. Typical examples include GroupDRO (Sagawa et al. 2020) and VREx (Krueger et al. 2021). The second is invariant representation learning. It aims to extract causal or stable features across domains. Representative methods include IRM (Arjovsky et al. 2019). Recent works such as SDL (Ye et al. 2023), FOOGD (Liao et al. 2024), and EVIL (Huang et al. 2025) build on these paradigms with new extensions.

However, directly applying these methods to TSC brings new challenges. Time series data are often non-stationary. They may contain long-term dependencies and concept drift (Wang et al. 2022; Wu et al. 2025). Current approaches mainly follow two directions. One is distribution alignment. It reduces domain gaps, as seen in AdaRNN (Du et al. 2021) and Diversify (Lu et al. 2023, 2024). The other is invariant feature separation. For example, GILE (Qian, Pan, and Miao 2021) separates core dynamics from temporal styles. ITSR (Shi et al. 2024) uses information theory to isolate label-relevant features. Many of these methods rely on internal constraints like orthogonality or independence. These constraints may not match the true data semantics. The learned invariance may not generalize beyond the training data. This leads to unreliable results under unseen distributions. A new mechanism is needed to guide models toward meaningful and stable representations.

Energy-Guided Representation Learning

Traditional disentanglement methods, such as those based on VAEs and GANs, commonly rely on regularization to enforce statistical independence in the latent space (Xia et al. 2023). However, this approach has inherent limitations. Such internal constraints do not guarantee that the learned factors will align with meaningful, real-world concepts. As a promising alternative, EBMs operate on a different principle. Instead of imposing indirect constraints, EBMs learn an energy function to directly model the probability density of the data. This direct modeling of data compatibility provides a powerful and highly flexible framework. Their broad applicability has been demonstrated in several advanced areas. For example, EOW-Softmax (Wang et al. 2021) uses EBMs for uncertainty calibration. ELI (Joseph et al. 2022) applies them in incremental learning. EGC (Guo et al. 2023) and the work by Golan et al. (Golan, Ganz, and Elad 2024) show their success in image generation and classification.

In the OOD field, a well-known use of EBMs is for OOD detection. A representative work (Liu et al. 2020) uses energy scores to identify whether a sample comes from an unseen distribution. Our framework takes a fundamentally different approach. We do not treat energy as a post hoc scoring

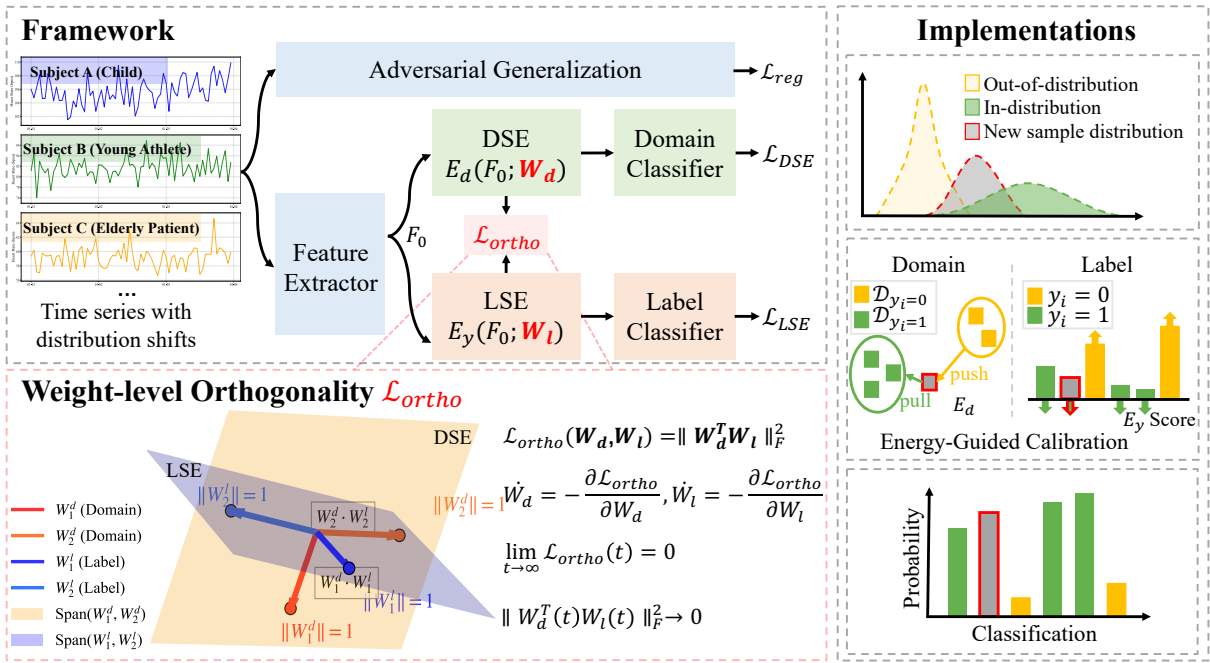


Figure 2: The **left upper** image provides an overview of ERIS framework, which comprises three branches: a domain-specific energy (DSE) branch, a label-specific energy (LSE) branch, and an auxiliary adversarial generalization (AG) branch. $E_d(\cdot)$ and $E_y(\cdot)$ represent energy function. The **left lower** image shows the weight-level orthogonality loss (\mathcal{L}_{ortho}), which enforces asymptotic orthogonality on the spaces of the domain and label projection matrices (**Lemma**, p. 4). The **right** image illustrates the implementation of the framework. Energy calibration facilitates semantically guided feature assignment by leveraging the contrast between low energy values for true domains/labels and high energy values for others, together with prototype distances.

function for detection. Instead, we use it as a guiding signal that is deeply integrated into the representation learning process. In short, ERIS transforms the role of energy from a detector to a guide.

Proposed Approach

The goal of ERIS is to perform guided disentanglement of learned representations, ensuring a clear separation between domain-specific and label-relevant features. This facilitates reliable OOD generalization in TSC. The overall architecture of ERIS is depicted in Figure 2.

Energy-Guided Calibration Mechanism

We obtain a shared representation, denoted as $F_0 \in \mathbb{R}^h$, from a shared feature extractor. Based on this representation, the energy-guided calibration mechanism employs two strategies: an energy-based semantic guidance and a weight-level orthogonality loss (see bottom left of Figure 2). The former is achieved by defining two types of learnable energy functions: domain-specific energy (E_d) and label-specific energy (E_y). These are parameterized functions that take the shared feature representation F_0 as input and map it to a scalar energy value. The parameters of these functions are learned to instill semantic guidance, where a lower energy value signifies a higher compatibility between the input features and the corresponding domain or label. Note that semantic guidance here refers to learned discriminative sig-

nals, not inherent properties of the data. We denote these functions as: $E_d = \mathcal{E}_d(F_0; \theta_d)$ and $E_y = \mathcal{E}_y(F_0; \theta_y)$, where $\mathcal{E}_d(\cdot)$ and $\mathcal{E}_y(\cdot)$ represent the energy functions parameterized by learnable weights θ_d and θ_y , respectively. Lower energy values E_d and E_y indicate better alignment with the target domain and label semantics, respectively. For both values, lower is better. We guide the function to quantify semantic guidance rooted in physical properties, such as the inherent differences in signal variance that exist across domains. To further enforce the separation, a weight-level orthogonality loss is applied to the projection matrices (W_d, W_l). This constraint ensures the domain and label subspaces are structurally independent, promoting a clean disentanglement.

Domain-Specific Energy (DSE). The objective is to assign lower energy to features originating from the true domain d_{true} , and higher energy to features under alternative domains. The DSE energy functions serve as indicators of how well a feature generalizes across different domains. Lower energy values indicate better generalization. To optimize these energy functions, DSE employs a contrastive structured loss defined as:

$$\mathcal{L}_{DSE} = \mathbb{E}_{(x,d) \sim \mathcal{D}_S} \left[E_d + \sum_{d' \neq d} \max(0, m_{\mathcal{D}} - E_{d'}) \right], \quad (1)$$

where $m_{\mathcal{D}}$ is an energy margin. This contrastive formulation encourages minimization of the energy for the true domain while pushing the energies associated with other domains above the margin, thereby enhancing the model's calibration

by learning to distinguish domain-specific features. Moreover, the DSE also models the domain-specific predictive uncertainty σ_d^2 and enforces that the confidence scores align with the negative energy values, which serve as proxies for domain match quality. This constraint can be formalized as: $\arg \max_{\{\sigma_d^2\}} \text{Correlation}(\text{Rank}(\|\sigma_d^2\|_2^{-1}), \text{Rank}(-E_d))$, where the operations are applied over all domains $d \in \mathcal{D}$, $\|\sigma_d^2\|_2$ denotes the norm of the variance vector, and $-E_d$ reflects the degree of domain match—the higher the value, the better the match. Although the DSE training loss does not directly optimize the ranking objective above, minimizing \mathcal{L}_{DSE} implicitly facilitates the learning of such ordinal relations in practice.

Label-Specific Energy with Prototype Congruence (LSE). The LSE is designed to enhance the model’s discriminative capability. Similar to DSE, LSE defines a set of label-specific energy functions, and incorporates class prototypes P_y to reinforce the consistency between features and their corresponding labels. It should be assigned a lower consistency energy if the input feature F_0 belongs to the ground-truth label y_{true} and lies close to its prototype $P_{y_{\text{true}}}$. To jointly quantify both label-specific energy and prototype distance, LSE can be defined as a consistency error function that $C_y := E_y + \|F_0 - P_y\|_2^2$. This function reflects how well the feature F_0 aligns with class y : smaller values indicate higher compatibility due to lower energy and closer proximity to the prototype.

The LSE loss comprises two components. The first is the label-wise contrastive loss:

$$\mathcal{L}_{\text{CL}} = \mathbb{E}_{(x,y) \sim \mathcal{D}_S} \left[E_y + \sum_{y' \neq y} \max(0, m_{L_1} - E_{y'}) \right]. \quad (2)$$

This objective encourages minimization of energy for the actual label while pushing incorrect label energies above a margin m_{L_1} . The second component is the prototype contrastive loss:

$$\mathcal{L}_{\text{Proto}} = \mathbb{E}_{(x,y) \sim \mathcal{D}_S} \left[\|F_0 - P_y\|_2^2 - \frac{1}{N_C - 1} \sum_{y' \neq y} (\|F_0 - P_{y'}\|_2^2 + m_{L_2}) \right]. \quad (3)$$

This loss encourages features to align closely with the actual class prototype and be distant from other class prototypes. The margin m_{L_2} controls the strength of repulsion.

The final LSE loss is given by:

$$\mathcal{L}_{\text{LSE}} = \mathcal{L}_{\text{CL}} + \mathcal{L}_{\text{Proto}}. \quad (4)$$

Through the minimization of \mathcal{L}_{LSE} , a link is established between low consistency error and high confidence, allowing for a structured representation of label-level fit quality. The resulting metric C_y is regarded as a calibrated measure of label compatibility, which serves to guide discriminative representation learning.

Weight-level Orthogonality Loss. In constructing the objective function, the original domain and label energy loss, are formulated using contrastive learning or energy minimization. When combined, these losses drive the two respective branches to focus on their tasks. However, this

alone does not guarantee that the subspaces learned by the two networks are mutually orthogonal. Their parameter spaces may still overlap, leading to interference between domain and label information. To address this, we introduce an orthogonality penalty term:

$$\mathcal{L}_{\text{ortho}}(\mathbf{W}_d, \mathbf{W}_l) = \|\mathbf{W}_d^T \mathbf{W}_l\|_F^2 = \sum_{ij} (\mathbf{W}_d, \mathbf{W}_l)_{ij}^2.$$

Unlike feature-level orthogonality (Qian, Pan, and Miao 2021; Shi et al. 2024), our framework enforces weight-level orthogonality. The key distinction lies in the scope of the constraint. Feature-level orthogonality is a per-instance constraint, enforced on the output features of each training sample. This can lead to brittle solutions that are sensitive to data shifts, as the underlying projection functions may remain correlated. In contrast, our weight-level orthogonality imposes a global structural guidance by directly making the model’s projection matrices $(\mathbf{W}_d, \mathbf{W}_l)$ orthogonal. This ensures the projection functions themselves are decorrelated, providing a more robust guarantee of feature separation for any input, including OOD samples. This term reaches its global minimum when $\mathbf{W}_d^T \mathbf{W}_l = 0$ and applies a quadratic penalty to any non-zero entries in the matrix. During optimization via gradient descent or its variants, this orthogonality penalty continuously pushes the updates in a direction that forces $\mathbf{W}_d^T \mathbf{W}_l$ tends to 0. This ensures that the column spaces of the two projection matrices, \mathbf{W}_d and \mathbf{W}_l , are driven towards orthogonality.

Lemma. Let $\mathbf{W}_d, \mathbf{W}_l \in \mathbb{R}^{h \times d}$ and define the weight-level orthogonality loss: $\mathcal{L}_{\text{ortho}}(\mathbf{W}_d, \mathbf{W}_l) = \|\mathbf{W}_d^T \mathbf{W}_l\|_F^2$. As shown in the lower-left part of Figure 2, the weight-level orthogonality loss decouples the parameter spaces of \mathbf{W}_d and \mathbf{W}_l by penalizing their non-zero inner product. Then $\mathcal{L}_{\text{ortho}}(t)$ is non-increasing along every trajectory and $\lim_{t \rightarrow \infty} \mathcal{L}_{\text{ortho}}(t) = 0$. Consequently $\|\mathbf{W}_d^T \mathbf{W}_l(t)\|_F$ tends to 0; in particular every non-degenerate ω -limit point $(\mathbf{W}_d^*, \mathbf{W}_l^*)$ satisfies the condition that $(\mathbf{W}_d^*, \mathbf{W}_l^*) = 0$.

Proof. Write the weight-level orthogonality loss in trace form, $\mathcal{L}_{\text{ortho}} = \text{Tr}[(\mathbf{W}_d^T \mathbf{W}_l)^T (\mathbf{W}_d^T \mathbf{W}_l)]$. Standard matrix calculus yields $\nabla_{\mathbf{W}_d} \mathcal{L}_{\text{ortho}} = 2\mathbf{W}_l \mathbf{W}_l^T \mathbf{W}_d$ and $\nabla_{\mathbf{W}_l} \mathcal{L}_{\text{ortho}} = 2\mathbf{W}_d \mathbf{W}_d^T \mathbf{W}_l$. Hence, the gradient flow can be written explicitly as: $\dot{\mathbf{W}}_d = -2\mathbf{W}_l \mathbf{W}_l^T \mathbf{W}_d$ and $\dot{\mathbf{W}}_l = -2\mathbf{W}_d \mathbf{W}_d^T \mathbf{W}_l$. The Frobenius inner product $\langle \mathbf{A}, \mathbf{B} \rangle = \text{Tr}(\mathbf{A}^T \mathbf{B})$ gives

$$\frac{d}{dt} \mathcal{L}_{\text{ortho}} = -4 \|\mathbf{W}_l \mathbf{W}_l^T \mathbf{W}_d\|_F^2 - 4 \|\mathbf{W}_d \mathbf{W}_d^T \mathbf{W}_l\|_F^2 \leq 0.$$

So $\mathcal{L}_{\text{ortho}}(t)$ is monotone decreasing and bounded below by 0; the limit $\mathcal{L}_{\infty} := \lim_{t \rightarrow \infty} \mathcal{L}_{\text{ortho}}(t)$ therefore exists. Assume for contradiction that \mathcal{L}_{∞} is greater than 0. Convergence of $\mathcal{L}_{\text{ortho}}(t)$ implies $\dot{\mathcal{L}}_{\text{ortho}}(t)$ that it tends to 0, which forces $\|\mathbf{W}_l \mathbf{W}_l^T \mathbf{W}_d\|_F^2$ and $\|\mathbf{W}_d \mathbf{W}_d^T \mathbf{W}_l\|_F^2$ to grow to 0. Choose a sequence t_k tends to infinite and set $\mathbf{A}_k := \mathbf{W}_l(t_k)^T \mathbf{W}_d(t_k)$. Because $\|\mathbf{W}_l(t_k) \mathbf{A}_k\|_F^2$ tends to 0 and $\mathbf{W}_l^T \mathbf{W}_l$ is positive semidefinite, multiplying on the left by $\mathbf{W}_l(t_k)^T$ and using the pseudo-inverse on its support yields $\|\mathbf{A}_k\|_F^2$ tends to 0. Hence, $\mathcal{L}_{\text{ortho}}(t_k) = \|\mathbf{A}_k\|_F^2$ tends to 0, contradicting \mathcal{L}_{∞} is greater than 0. Thus, \mathcal{L}_{∞} equals 0,

and the claimed limit follows. Any ω -limit point must satisfy $W_l^T W_d = 0$ because $\mathcal{L}_{\text{ortho}}$ is continuous. With the minimization of the orthogonality loss, the feature representations produced by the domain (DSE) and label (LSE) branches are gradually driven toward asymptotic orthogonality in the latent space. Consequently, label information is effectively separated from domain-specific variations.

Adversarial Generalization (AG)

We propose adversarial generalization (AG), a mechanism designed to foster robust and generalizable representations through a two-fold adversarial strategy. Firstly, to achieve global alignment, it employs an adversarial game where a feature extractor is trained to deceive a domain discriminator. This forces the learned features to become domain-indistinguishable, thereby aligning distributions across different domains. Secondly, to enhance local robustness, AG smooths the latent feature space. It identifies an adversarial perturbation r_{adv} that maximally alters the model’s predictive distribution: $r_{\text{adv}} := \arg \max D_{\text{KL}}(p(y | h, \hat{\theta}) \| p(y | h + r, \hat{\theta}))$. Subsequently, the model is trained to be resilient against this perturbation by minimizing the regularization loss:

$$\mathcal{L}_{\text{reg}} = D_{\text{KL}}(p(y | h, \hat{\theta}) \| p(y | h + r_{\text{adv}}, \theta)). \quad (5)$$

By synergizing global domain alignment with local adversarial smoothing, AG produces representations that are both domain-agnostic and locally invariant, leading to superior generalization under distribution shifts.

Model Summary

In summary, we adopt an end-to-end training strategy where the total loss function is defined as a weighted sum of the individual objectives:

$$\mathcal{L}_{\text{total}} = \lambda_1 \mathcal{L}_{\text{DSE}} + \lambda_2 \mathcal{L}_{\text{LSE}} + \mathcal{L}_{\text{ortho}} + \mathcal{L}_{\text{reg}}, \quad (6)$$

where λ_1 and λ_2 are the trade-off parameters between the loss functions. Empirically, we set a relatively small λ_1 and a larger λ_2 , so that the prototype-based LSE loss dominates the learning process to ensure strong classification performance under unseen or OOD settings. During inference, no additional computation of the auxiliary and orthogonality loss terms is required, significantly simplifying the deployment phase. Due to space constraints, the complexity analysis is included in the Appendix.

Experiments

Experimental Settings

Datasets. We perform experiments on four large sensor benchmark datasets, each containing multiple domains and labels. The four datasets used in the experiments are UCIHAR (Anguita et al. 2012), UniMiB-SHAR (Hnoohom, Mekruksavanich, and Jitpattanakul 2017), Opportunity (Roggen et al. 2010; Chavarriaga et al. 2013), and EMG (Lobov et al. 2018), providing a comprehensive assessment of ERIS’s OOD generalization performance. Detailed descriptions and processing are provided in the Appendix.

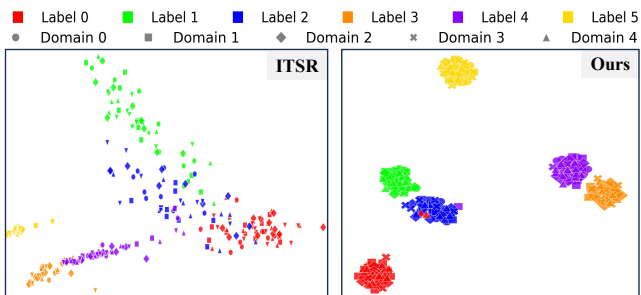


Figure 3: Visualization of t-SNE comparing ITSR and ours ERIS on the UCIHAR dataset.

Implementation Details. We evaluate the ERIS and baselines on a server equipped with two NVIDIA GeForce RTX 3090 GPUs, each with 24GB of memory. The server supports CUDA 12.8, with the code implemented in PyTorch 2.7.0. To reduce experimental variability, we conduct five independent runs for each experiment on both the general models and the OOD models specifically designed for time series, reporting the average results along with the standard deviation. Additionally, we provide the average ranking results for each domain on four datasets. More details and baselines are provided in the Appendix.

Main Results

Overall Performance. The superior capabilities of the ERIS model are demonstrated through a combined analysis of Tables 1 and 2. In terms of generalization, it is shown in Table 1 that other SOTA methods are significantly outperformed by ERIS. The highest average accuracy of 75.47% and the best average rank of 1.31 are achieved. Strong cross-domain capabilities are thereby demonstrated. Further strengths are shown in Table 2, where ERIS is compared with other EBMs. A leading position in accuracy was secured. Moreover, the lowest ECE of 0.12 is also achieved. This crucial result indicates that the model’s confidence is more reliable, and issues of overconfidence are mitigated. This leading performance is supported by robust statistical evidence. The Wilcoxon signed-rank test was used to confirm statistical significance. For all comparisons (with **all p-values < 0.05**), confirming that the observed performance gains are not due to chance. Furthermore, ERIS exhibits robust adaptability in OOD tasks, effectively adjusting to different task requirements, which further enhances its generalization capabilities. Finally, ERIS proves to be highly effective in handling complex tasks, with minimal fluctuation in results across various datasets and models.

Visualization. In Figure 3, we compare the latest time series OOD generalization model using T-SNE on the UCIHAR dataset. We observe that, compared to the ITSR, our ERIS is better at separating different domains and labels, with more precise label boundaries and fewer overlapping regions. This indicates that our ERIS has a stronger capability in handling the heterogeneity between different domains.

Datasets	Target Domain	ERIS (Ours)	Time Series OOD Generalization				General OOD Generalization				
			GILE	AdaRNN	Diversify	ITSR	GroupDRO	VREx	SDL	FOOGD	EVIL
			AAAI '21	CIKM'21	ICLR'23	KDD'24	ICLR'20	ICML'21	AAAI '23	NeurIPS'24	IJCV'25
UCIHAR	0	94.70 ± 1.20	79.38 ± 1.63	82.83 ± 1.64	79.25 ± 5.01	78.80 ± 5.58	92.34 ± 1.24	93.03 ± 0.88	85.25 ± 2.89	92.71 ± 2.05	89.31 ± 2.88
	1	84.37 ± 2.17	75.63 ± 0.95	60.80 ± 5.73	55.77 ± 6.40	80.67 ± 4.65	71.33 ± 1.80	72.92 ± 2.40	61.60 ± 3.38	80.07 ± 1.57	70.82 ± 6.97
	2	95.05 ± 1.00	85.73 ± 0.73	91.91 ± 2.34	78.13 ± 4.61	93.61 ± 2.44	91.97 ± 0.99	92.32 ± 0.77	92.38 ± 1.08	92.49 ± 1.05	93.30 ± 2.00
	3	94.39 ± 2.84	91.13 ± 1.86	69.85 ± 4.23	66.44 ± 4.45	86.06 ± 2.73	86.69 ± 5.15	87.01 ± 4.15	75.34 ± 8.72	85.98 ± 4.70	83.95 ± 3.76
	4	97.42 ± 0.98	87.25 ± 2.11	81.86 ± 3.43	73.91 ± 3.16	91.33 ± 2.88	94.24 ± 5.49	93.65 ± 4.45	82.59 ± 1.28	91.70 ± 2.40	92.16 ± 3.42
	Avg. Acc	93.19 ± 4.91	83.82 ± 5.87	77.45 ± 11.63	70.70 ± 9.93	86.09 ± 6.87	87.32 ± 9.14	87.79 ± 8.41	79.43 ± 11.42	88.59 ± 5.59	85.91 ± 9.20
Avg. Rank	1.00	6.00	8.40	9.80	5.00	4.60	3.80	7.00	4.20	5.20	
UniMiB-SHAR	1	59.59 ± 0.95	46.93 ± 1.55	34.95 ± 5.66	50.94 ± 3.21	51.67 ± 2.67	43.91 ± 1.86	43.91 ± 2.27	42.71 ± 2.41	55.02 ± 7.13	45.37 ± 1.50
	2	49.34 ± 0.83	47.97 ± 2.26	36.23 ± 5.58	46.04 ± 3.25	50.60 ± 4.42	38.60 ± 1.60	39.87 ± 1.38	41.48 ± 2.36	47.99 ± 3.11	45.42 ± 3.01
	3	70.60 ± 1.59	66.82 ± 1.62	39.41 ± 8.17	57.70 ± 2.74	58.95 ± 7.37	64.28 ± 1.66	65.92 ± 1.18	64.68 ± 0.92	66.57 ± 4.30	64.53 ± 2.81
	5	41.41 ± 0.81	37.38 ± 1.27	33.96 ± 7.73	41.68 ± 1.89	43.15 ± 2.14	39.67 ± 0.61	39.87 ± 1.57	38.73 ± 1.88	43.41 ± 5.83	39.28 ± 2.88
	Avg. Acc	55.23 ± 11.30	49.77 ± 11.06	36.14 ± 6.66	49.09 ± 6.64	51.10 ± 7.15	46.61 ± 10.75	47.39 ± 11.21	46.90 ± 10.79	53.25 ± 10.21	48.65 ± 10.04
	Avg. Rank	2.00	5.25	10.0	5.25	3.50	7.25	6.50	7.50	2.00	5.75
EMG	0	73.59 ± 1.84	39.27 ± 4.19	52.09 ± 3.18	48.99 ± 4.97	67.17 ± 1.99	44.50 ± 3.24	45.03 ± 3.11	43.96 ± 3.52	56.93 ± 8.52	61.63 ± 8.25
	1	49.11 ± 2.58	38.57 ± 6.12	44.09 ± 1.36	42.52 ± 6.66	48.80 ± 3.71	38.54 ± 1.95	38.64 ± 1.87	39.59 ± 1.98	45.88 ± 7.17	47.38 ± 5.30
	2	65.12 ± 6.20	40.45 ± 1.99	57.68 ± 2.81	45.12 ± 5.25	62.21 ± 2.06	39.31 ± 1.52	39.30 ± 0.67	38.26 ± 0.76	59.84 ± 7.72	51.68 ± 6.21
	3	85.87 ± 1.55	50.85 ± 1.81	54.62 ± 3.85	63.85 ± 6.52	82.89 ± 1.26	49.43 ± 2.56	48.37 ± 2.30	47.79 ± 1.39	77.91 ± 5.78	60.40 ± 8.44
	Avg. Acc	68.42 ± 14.11	42.28 ± 6.27	52.12 ± 5.84	50.12 ± 10.05	65.27 ± 12.71	42.94 ± 5.02	42.84 ± 4.61	42.40 ± 4.35	60.14 ± 13.61	55.27 ± 8.99
	Avg. Rank	1.00	8.25	5.00	5.50	2.00	8.50	8.25	9.00	3.50	4.00
Opportunity	S1	82.22 ± 0.16	83.06 ± 0.42	80.59 ± 0.62	79.37 ± 0.35	80.97 ± 0.39	74.84 ± 2.67	75.30 ± 2.46	75.01 ± 0.57	81.31 ± 1.31	72.90 ± 7.66
	S2	81.10 ± 0.28	81.05 ± 0.23	80.27 ± 0.44	77.80 ± 0.75	79.84 ± 0.45	74.95 ± 1.86	74.90 ± 1.78	73.51 ± 0.85	79.91 ± 1.22	74.03 ± 4.94
	S3	77.65 ± 0.11	77.62 ± 0.50	74.31 ± 0.52	73.68 ± 1.29	76.19 ± 0.57	75.98 ± 0.55	73.80 ± 1.46	75.11 ± 0.27	75.18 ± 3.31	74.59 ± 2.89
	S4	82.25 ± 0.13	81.32 ± 0.65	79.68 ± 0.27	79.12 ± 0.34	81.01 ± 0.62	75.79 ± 0.85	75.97 ± 0.60	74.97 ± 0.30	78.42 ± 3.73	77.75 ± 3.47
	Avg. Acc	80.81 ± 1.94	80.76 ± 2.19	78.71 ± 2.67	77.49 ± 2.45	79.61 ± 2.15	75.39 ± 1.65	74.99 ± 1.77	74.65 ± 0.85	78.70 ± 3.37	74.82 ± 5.02
	Avg. Rank	1.25	1.75	5.00	6.75	3.75	7.25	8.00	8.50	4.50	8.25
Avg. ALL	75.47	65.34	62.06	62.37	71.43	64.49	64.69	61.93	71.25	67.32	
p -value	-	$\leq 1e-4$	$\leq 1e-4$	$\leq 1e-4$	$\leq 1e-4$	$\leq 1e-4$	$\leq 1e-4$	$\leq 1e-4$	$\leq 1e-4$	$\leq 1e-4$	

Table 1: Overall comparison results of ERIS and other methods across four datasets (%). ‘Avg.’ is short for average, and the best performance is in **bold**. ‘Avg. Rank’ is determined by summing the ranks in each dataset and dividing the total by the number of datasets considered. ‘Avg. ALL’ represents the average accuracy across all datasets. The p -value is obtained using the Wilcoxon signed-rank test; a value less than 0.05 indicates that the performance difference between ERIS and the compared method is statistically significant.

Datasets	ERIS (Ours)		EOW-Softmax ICCV'21		ELI CVPR'22		EGC ICCV'23		Golan NeurIPS'24	
	ACC (\uparrow)	ECE (\downarrow)	ACC (\uparrow)	ECE (\downarrow)	ACC (\uparrow)	ECE (\downarrow)	ACC (\uparrow)	ECE (\downarrow)	ACC (\uparrow)	ECE (\downarrow)
UCIHAR	93.19 ± 4.91	0.07 ± 0.03	92.51 ± 4.36	0.09 ± 0.04	84.28 ± 4.39	0.43 ± 0.06	82.78 ± 5.90	0.45 ± 0.09	82.86 ± 5.01	0.26 ± 0.11
UniMiB-SHAR	55.23 ± 11.30	0.17 ± 0.11	53.09 ± 12.04	0.25 ± 0.12	34.60 ± 4.61	0.21 ± 0.05	23.50 ± 13.58	0.37 ± 0.13	32.02 ± 9.82	0.21 ± 0.12
EMG	68.42 ± 14.11	0.20 ± 0.12	63.17 ± 12.86	0.26 ± 0.13	45.33 ± 6.96	0.21 ± 0.07	42.75 ± 12.08	0.41 ± 0.14	57.13 ± 9.29	0.28 ± 0.08
Opportunity	80.81 ± 1.94	0.06 ± 0.03	80.15 ± 2.23	0.08 ± 0.03	79.81 ± 2.82	0.12 ± 0.02	73.93 ± 3.30	0.29 ± 0.16	78.35 ± 2.14	0.12 ± 0.03
Avg. ALL	75.47	0.12	73.42	0.17	62.37	0.26	57.33	0.39	63.78	0.22
p -value	-	-	$\leq 1e-4$	$\leq 1e-4$	$\leq 1e-4$	$\leq 1e-4$	$\leq 1e-4$	$\leq 1e-4$	$\leq 1e-4$	$\leq 1e-4$

Table 2: Performance comparison of energy-based methods. The result is the average of all target domains on each dataset. ECE stands for expected calibration error. The p -value is obtained using the Wilcoxon signed-rank test.

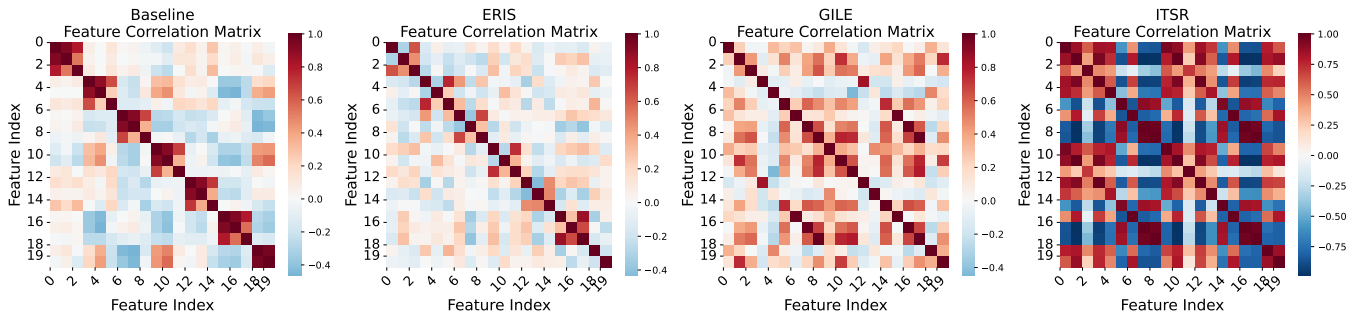


Figure 4: Feature correlation matrices for different orthogonal methods on the UCIHAR dataset visualize pairwise feature correlations. Red shows positive correlations (darker for stronger), blue indicates negative correlations, and white represents no correlation.

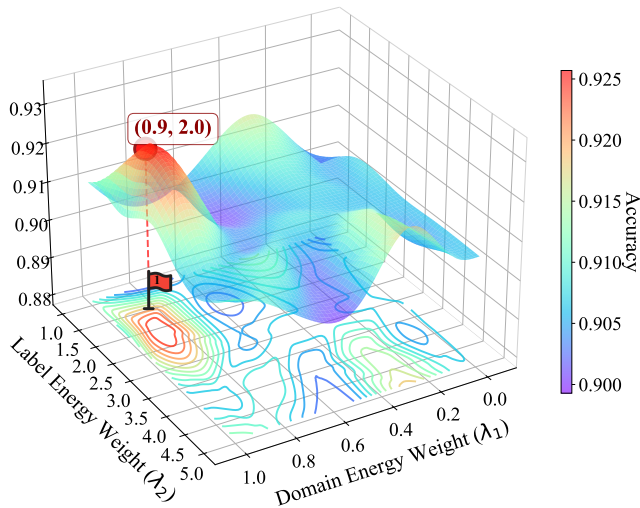


Figure 5: The results of ERIS on the UCIHAR dataset vary with changes in the parameters λ_1 and λ_2 .

Ablation Studies

How do the orthogonality methods affect the performance? We evaluate how existing models impacted the correlation of the TSMixer (Chen et al. 2023) baseline. In Figure 4, ERIS adapts better to new devices or environments when handling OOD scenarios. The feature correlation matrix is clearer and more dispersed, with the correlation coefficients concentrated within 0.1, directly minimizing the correlations. In contrast, GILE presents an overly concentrated block structure, while ITSR exhibits a checkerboard pattern of strong positive and negative correlations, with higher regularity. However, compared to ERIS, ITSR may overly constrain the relationships between features in its pursuit of feature orthogonality. The orthogonalized mutual information matrix analysis for Figure 4 is provided in the Appendix. Overall, ERIS performs the best, highlighting the superior results of its semantically guided disentanglement.

How does the loss weighting factor affect the performance? We conduct experiments on the UCIHAR dataset with different parameter settings, based on Eq. (6). Empir-

Index	DSE	LSE	AR	ACC	F1	Precision	Recall
A	✓	✗	✗	80.50	79.30	84.18	80.30
B	✗	✓	✗	81.81	80.80	84.64	81.58
C (w/o \mathcal{L}_{ortho})	✓	✓	✗	84.16	82.88	87.43	83.71
D (w/ \mathcal{L}_{ortho})	✓	✓	✗	85.69	86.50	88.80	87.95
E	✗	✓	✓	85.33	84.17	88.22	85.13
F (w/o \mathcal{L}_{ortho})	✓	✓	✓	89.29	88.43	90.50	88.79
G (w/ \mathcal{L}_{ortho})	✓	✓	✓	91.51	90.31	92.54	90.46

Table 3: Ablation results of ours ERIS. All metrics are averaged across five target domains of the UCIHAR dataset.

ically, as shown in Figure 5, we set a smaller value for λ_1 to 0.9 and a larger value for λ_2 to 2. A larger λ_2 strongly guides the model to optimize the LSE process using class prototypes. It encourages features to cluster around their correct prototypes and stay away from others. This creates clear and discriminative class boundaries. As a result, the model separates label information from domain-specific variations.

Component analysis. In Table 3, we present an ablation study of the different components. Removing DSE, LSE, or AR results in a performance drop, with the removal of AR having a notably negative impact on accuracy and F1 score. The AR is essential for local perturbation robustness, guaranteeing stable performance under distribution shifts. Ultimately, configuration (G) achieves the best performance.

Conclusion

In this work, we observe that the unguided nature of feature separation leads to overly entangled domain relationships, which hinder the model’s ability to learn invariant features. To address this issue, we propose ERIS, a framework that enhances the disentanglement of domain-specific and label-relevant features through three key mechanisms: an energy-guided calibration mechanism, a weight-level orthogonality strategy, and an auxiliary adversarial generalization branch. We theoretically and empirically demonstrate that the orthogonality strategy not only reduces interference among features but also preserves the discriminative power and information integrity of label-relevant representations.

Furthermore, we analyze the impact of the weight-level orthogonality strategy across various baselines. Experimental results demonstrate that ERIS significantly outperforms SOTA methods and highlights its effectiveness in alleviating domain and label entanglement. Future work may further investigate the theoretical boundaries of energy-based modeling in the context of temporal uncertainty.

References

- Anguita, D.; Ghio, A.; Oneto, L.; Parra, X.; and Reyes-Ortiz, J. L. 2012. Human Activity Recognition on Smartphones Using a Multiclass Hardware-friendly Support Vector Machine. In *Proceedings of the International Workshop on Ambient Assisted Living (IWAAL)*, 216–223. Springer.
- Arjovsky, M.; Bottou, L.; Gulrajani, I.; and Lopez-Paz, D. 2019. Invariant Risk Minimization. *arXiv preprint arXiv:1907.02893*.
- Chavarriaga, R.; Sagha, H.; Calatroni, A.; Digumarti, S. T.; Tröster, G.; Millán, J. d. R.; and Roggen, D. 2013. The Opportunity Challenge: A Benchmark Database for On-body Sensor-based Activity Recognition. *Pattern Recognition Letters*, 34(15): 2033–2042.
- Chen, S.-A.; Li, C.-L.; Arik, S. O.; Yoder, N. C.; and Pfister, T. 2023. TSMixer: An All-MLP Architecture for Time Series Forecasting. *Transactions on Machine Learning Research*.
- Chowdhury, R. R.; Zhang, X.; Shang, J.; Gupta, R. K.; and Hong, D. 2022. TARNet: Task-Aware Reconstruction for Time-series Transformer. In *Proceedings of the ACM SIGKDD conference on knowledge discovery and data Mining (KDD)*, 212–220.
- Du, Y.; Wang, J.; Feng, W.; Pan, S.; Qin, T.; Xu, R.; and Wang, C. 2021. AdaRNN: Adaptive Learning and Forecasting of Time Series. In *ACM International Conference on Information and Knowledge Management (CIKM)*, 402–411.
- Golan, S.; Ganz, R.; and Elad, M. 2024. Enhancing Consistency-based Image Generation via Adversarially-trained Classification And Energy-based Discrimination. volume 37, 47966–47986.
- Guo, Q.; Ma, C.; Jiang, Y.; Yuan, Z.; Yu, Y.; and Luo, P. 2023. EGC: Image Generation And Classification via A Diffusion Energy-based Model. In *Proceedings of the IEEE/CVF International Conference on Computer Vision (ICCV)*, 22952–22962.
- Gupta, A.; Gupta, H. P.; Biswas, B.; and Dutta, T. 2020. Approaches and Applications of Early Classification of Time Series: A Review. *IEEE Transactions on Artificial Intelligence*, 1(1): 47–61.
- Gupta, S.; Sutar, V.; Singh, V.; and Sethi, A. 2025. FedAlign: Federated Domain Generalization with Cross-Client Feature Alignment. In *Proceedings of the Computer Vision and Pattern Recognition Conference (CVPR)*, 1801–1810.
- Hendrycks, D.; Basart, S.; Mu, N.; Kadavath, S.; Wang, F.; Dorundo, E.; Desai, R.; Zhu, T.; Parajuli, S.; Guo, M.; et al. 2021. The Many Faces of Robustness: A Critical Analysis of Out-of-distribution Generalization. In *Proceedings of the IEEE/CVF International Conference on Computer Vision (CVPR)*, 8340–8349.
- Hnoohom, N.; Mekruksavanich, S.; and Jitpattanakul, A. 2017. Human Activity Recognition Using Triaxial Acceleration Data from Smartphone and Ensemble Learning. In *Proceedings of the International Conference on Signal-image Technology and Internet-based Systems (SITIS)*, 408–412. IEEE.
- Huang, Z.; Li, M.; Shen, L.; Yu, J.; Gong, C.; Han, B.; and Liu, T. 2025. Winning Prize Comes from Losing Tickets: Improve Invariant Learning by Exploring Variant Parameters for Out-of-distribution Generalization. *International Journal of Computer Vision*, 133(1): 456–474.
- Jian, C.; Yang, K.; and Jiao, Y. 2024. Tri-Level Navigator: LLM-Empowered Tri-Level Learning for Time Series OOD Generalization. In *Proceedings of the Advances in Neural Information Processing Systems (NeurIPS)*, volume 37, 110613–110642.
- Joseph, K.; Khan, S.; Khan, F. S.; Anwer, R. M.; and Balasubramanian, V. N. 2022. Energy-based Latent Aligner for Incremental Learning. In *Proceedings of the IEEE/CVF Conference on Computer Vision and Pattern Recognition (CVPR)*, 7452–7461.
- Kaur, R.; Sridhar, K.; Park, S.; Yang, Y.; Jha, S.; Roy, A.; Sokolsky, O.; and Lee, I. 2023. Codit: Conformal out-of-distribution detection in time-series data for cyber-physical systems. In *Proceedings of the ACM/IEEE 14th International Conference on Cyber-Physical Systems (CPS-IoT)*, 120–131.
- Krueger, D.; Caballero, E.; Jacobsen, J.-H.; Zhang, A.; Binias, J.; Zhang, D.; Le Priol, R.; and Courville, A. 2021. Out-of-distribution Generalization via Risk Extrapolation (REX). In *Proceedings of the International Conference on Machine Learning (ICML)*, 5815–5826. PMLR.
- LeCun, Y.; Chopra, S.; Hadsell, R.; Ranzato, M.; Huang, F.; et al. 2006. A Tutorial on Energy-based Learning. *Predicting Structured Data*, 1(0).
- Li, W.; Ma, Y.; Shao, K.; Yi, Z.; Cao, W.; Yin, M.; Xu, T.; and Wu, X. 2024. The Human-machine Interface Design Based on sEMG And Motor Imagery EEG for Lower Limb Exoskeleton Assistance System. *IEEE Transactions on Instrumentation and Measurement*, 73: 1–14.
- Li, Z.; Cai, R.; Chen, G.; Sun, B.; Hao, Z.; and Zhang, K. 2023. Subspace Identification for Multi-source Domain Adaptation. In *Proceedings of the Advances in Neural Information Processing Systems (NeurIPS)*, volume 36, 34504–34518.
- Liao, X.; Liu, W.; Zhou, P.; Yu, F.; Xu, J.; Wang, J.; Wang, W.; Chen, C.; and Zheng, X. 2024. Foogd: Federated Collaboration for Both Out-of-Distribution Generalization and Detection. In *Proceedings of the Advances in Neural Information Processing Systems (NeurIPS)*, volume 37, 132908–132945.
- Liu, W.; Wang, X.; Owens, J.; and Li, Y. 2020. Energy-based Out-of-distribution Detection. In *Proceedings of the Advances in Neural Information Processing Systems (NeurIPS)*, volume 33, 21464–21475.

- Lobov, S.; Krilova, N.; Kastalskiy, I.; Kazantsev, V.; and Makarov, V. A. 2018. Latent Factors Limiting the Performance of sEMG-interfaces. *Sensors*, 18(4): 1122.
- Lu, W.; Wang, J.; Sun, X.; Chen, Y.; Ji, X.; Yang, Q.; and Xie, X. 2024. Diversify: A General Framework for Time Series Out-of-Distribution Detection and Generalization. *IEEE Transactions on Pattern Analysis and Machine Intelligence*, 46(6): 4534–4550.
- Lu, W.; Wang, J.; Sun, X.; Chen, Y.; and Xie, X. 2023. Out-of-Distribution Representation Learning for Time Series Classification. In *Proceedings of the International Conference on Learning Representations (ICLR)*.
- Mu, Y.; Shahzad, M.; and Zhu, X. X. 2025. MPTSNet: Integrating multiscale periodic local patterns and global dependencies for multivariate time series classification. In *Proceedings of the AAAI Conference on Artificial Intelligence*, volume 39, 19572–19580.
- Nie, Y.; Nguyen, N. H.; Sinthong, P.; and Kalagnanam, J. 2023. A Time Series is Worth 64 Words: Long-term Forecasting with Transformers. In *Proceedings of the International Conference on Learning Representations (ICLR)*.
- Qian, H.; Pan, S. J.; and Miao, C. 2021. Latent Independent Excitation for Generalizable Sensor-based Cross-person Activity Recognition. In *Proceedings of the AAAI Conference on Artificial Intelligence (AAAI)*, volume 35, 11921–11929.
- Roggen, D.; Calatroni, A.; Rossi, M.; Holleczeck, T.; Förster, K.; Tröster, G.; Lukowicz, P.; Bannach, D.; Pirkl, G.; Ferscha, A.; et al. 2010. Collecting Complex Activity Datasets in Highly Rich Networked Sensor Environments. In *Proceedings of the International Conference on Networked Sensing Systems (INSS)*, 233–240. IEEE.
- Sagawa, S.; Koh, P. W.; Hashimoto, T. B.; and Liang, P. 2020. Distributionally Robust Neural Networks. In *Proceedings of the International Conference on Learning Representations (ICLR)*.
- Shi, R.; Huang, H.; Yin, K.; Zhou, W.; and Jin, H. 2024. Orthogonality Matters: Invariant Time Series Representation for Out-of-Distribution Classification. In *Proceedings of the ACM SIGKDD Conference on Knowledge Discovery and Data Mining (KDD)*, 2674–2685.
- Wang, J.; Lan, C.; Liu, C.; Ouyang, Y.; Qin, T.; Lu, W.; Chen, Y.; Zeng, W.; and Yu, P. S. 2022. Generalizing to Unseen Domains: A Survey on Domain Generalization. *IEEE Transactions on Knowledge and Data Engineering*, 35(8): 8052–8072.
- Wang, Y.; Li, B.; Che, T.; Zhou, K.; Liu, Z.; and Li, D. 2021. Energy-Based Open-World Uncertainty Modeling for Confidence Calibration. In *Proceedings of the IEEE/CVF International Conference on Computer Vision (ICCV)*, 9282–9291.
- Wang, Y.; Xu, Y.; Yang, J.; Wu, M.; Li, X.; Xie, L.; and Chen, Z. 2024. Graph-Aware Contrasting for Multivariate Time-series Classification. In *Proceedings of the AAAI conference on artificial intelligence (AAAI)*, volume 38, 15725–15734.
- Wu, X.; Teng, F.; Li, X.; Zhang, J.; Li, T.; and Duan, Q. 2025. Out-of-Distribution Generalization in Time Series: A Survey. *arXiv preprint arXiv:2503.13868*.
- Xia, W.; Zhang, Y.; Yang, Y.; Xue, J.-H.; Zhou, B.; and Yang, M.-H. 2023. GAN Inversion: A Survey. *IEEE Transactions on Pattern Analysis and Machine Intelligence*, 45(3): 3121–3138.
- Ye, N.; Zhu, L.; Wang, J.; Zeng, Z.; Shao, J.; Peng, C.; Pan, B.; Li, K.; and Zhu, J. 2023. Certifiable Out-of-Distribution Generalization. In *Proceedings of the AAAI Conference on Artificial Intelligence (AAAI)*, volume 37, 10927–10935.

A Complexity analysis

Let the input time series length be N , and the per-timestep channel dimension be d_{in} . The input is first processed by L layers of 1D convolution, where each layer uses kernel size K , and outputs C_l channels. The resulting feature maps are then aggregated via global pooling (or flattening), producing an encoding vector $x \in \mathbb{R}^{1 \times b}$. Two separate 3-layer MLPs, each with a hidden width of h , are used for the label and domain branches, respectively. Their output dimensions correspond to the number of labels, N_y , and the number of domains, N_d .

Time. The convolutional encoding phase consumes $O(LNKC^2)$ under uniform configurations. Next, the two 3-layer MLPs perform forward propagation, incurring a combined cost of:

$$O(bh + h^2 + h(N_y + N_d)). \quad (7)$$

Combining both parts and dropping lower-order constants yields an overall forward-pass complexity of:

$$O(LNKC^2 + bh + h^2 + h(N_y + N_d)). \quad (8)$$

As the output layer cost $h(N_y + N_d)$ is typically dominated by h^2 , we simplify the expression to:

$$O(LNKC^2 + h(b + h)). \quad (9)$$

Space. Model parameters consist of the convolution kernels, requiring $O(LNKC^2)$, and the MLP weights, contributing

$$O(bh + h^2 + h(N_y + N_d)). \quad (10)$$

For dynamic memory, the model needs to store the input sequence $O(N)$, the encoded feature $O(b)$, and the output tensors $O(2N_y + 2N_d)$. As with time complexity, $h(N_y + N_d)$ is typically absorbed into h^2 , resulting in the final space complexity:

$$O(LNKC^2 + h(b + h) + N + b). \quad (11)$$

B Experiments

B.1 Datasets

We provide a detailed introduction to the four datasets utilized in our work. Their summaries are provided in **Table 4**.

- **The UCI Human Activity Recognition (UCIHAR)** (Anguita et al. 2012) dataset is a comprehensive collection of smartphone sensor data designed to classify everyday human activities. Participants in the study wore smartphones that recorded data from both accelerometers and gyroscopes, capturing 6 distinct activities: walking, walking up stairs, walking down stairs, sitting, standing, and lying down. The dataset features a sampling frequency of 50 Hz and contains 1,609 time series samples, with each sample having an initial feature dimension of 9. The primary classification task is to accurately identify which of the 6 activities a user is performing based on the sensor data. The UCIHAR dataset is logically divided into 5 distinct domains, with each domain comprising data from 6 volunteers, ensuring a diverse representation of activity patterns.

Datasets	Samples	Channels	Classes	Domains
UCIHAR	1,609	9	6	5
UniMiB-SHAR	1,569	453	17	4
Opportunity	869,387	77	18	4
EMG	6,883	200	6	4

Table 4: Summary of four datasets.

- **The University of Milano-Bicocca Smartphone-Based Human Activity Recognition (UniMiB-SHAR)** (Hnoohom, Mekruksavanich, and Jitpattanukul 2017) dataset is a specialized collection of accelerometer data from Android smartphones, designed for both human activity recognition and fall detection. It encompasses 11,771 samples from 30 participants aged 18 to 60, with data collected from 3 smartphone sensors at a sampling frequency of 50 Hz. The dataset meticulously categorizes activities into 17 fine-grained classes, specifically 9 activities of daily living and 8 distinct fall types. For evaluation, the dataset is organized into four common domains, resulting in a total of 1,569 time series data samples, each characterized by 453 features derived from the 3 sensors.
- **The Electromyography (EMG)** (Lobov et al. 2018) dataset is a collection of electromyographic signals, a standard bioelectrical signal, designed for the task of classifying six different hand gestures. It includes 6,883 time series samples, with each sample containing EMG signals from 8 channels, where each channel has a feature dimension of 200. The data was collected from 36 volunteers and is organized into 4 distinct domains, with each domain comprising nine individuals. This dataset is particularly suitable for OOD generalization research because EMG signals are susceptible to various influencing factors during data collection. These include variations in acquisition equipment, environmental conditions, and individual physiological differences.
- **The Opportunity** (Roggen et al. 2010) dataset, sampled at 30 Hz and comprising 869,237 time series samples (each with 77 dimensions), is a sensor-based collection for human activity recognition. It features 4 participants performing 18 daily activities in a home setting (e.g., opening drawers, refrigerators, doors). This dataset, a subset of the Opportunity UCI dataset (Chavarriaga et al. 2013), uniquely incorporates data from various internal sensors and deploys multiple wearable devices and environmental sensors to collect multimodal somatosensory data during daily activities, covering a range of behavioral samples from basic motion primitives to high-level interactive gestures.

B.2 Experimental Baselines

To comprehensively evaluate the performance of the ERIS method, we establish a multi-dimensional experimental framework and conduct rigorous comparisons against a set of representative baseline approaches.

- **Time Series and General OOD Generalization Baselines:** The evaluation is structured along two primary dimensions. The first dimension focuses on direct competitors tailored for time series data. Specifically, we consider GILE (Qian, Pan, and Miao 2021), which employs generative invariant learning; AdaRNN (Du et al. 2021), which introduces adaptive recurrent network structures; Diversify (Lu et al. 2023), which enhances generalization through synthetic domain augmentation; and ITSR (Shi et al. 2024), which learns invariant representations in the time-frequency domain. The second dimension assesses the broader applicability of ERIS’s underlying principles by comparing it with general OOD frameworks. These include GroupDRO (Sagawa et al. 2020), which minimizes worst-case group risk; VREx (Krueger et al. 2021), which promotes generalization via risk variance regularization; SDL (Ye et al. 2023), which learns invariant features by decoupling spectral representations; and recent cutting-edge methods such as FOOOD (Liao et al. 2024) and EVIL (Huang et al. 2025).
- **General Energy-based Baselines:** From a methodological standpoint, ERIS is formulated as an energy-based model (EBM). Due to the absence of existing energy-based generalization methods specifically designed for time series data, we conduct orthogonal experiments using representative EBM approaches developed in other fields. These include EOW-Softmax (Wang et al. 2021), ELI (Joseph et al. 2022), EGC (Guo et al. 2023), and Golan (Golan, Ganz, and Elad 2024). This set of experiments evaluates not only classification accuracy but also expected calibration error (ECE), a key metric for assessing the reliability of model confidence. This provides deeper insights into ERIS’s ability to produce both accurate and well-calibrated predictions.
- **General Time Series Classification Baselines:** To establish robust performance baselines and to quantify the performance improvements brought by ERIS over standard models, we further compare it against a set of representative SOTA time series classification methods. These include TARNet (Chowdhury et al. 2022), PatchTST (Nie et al. 2023), TS-GAC (Wang et al. 2024), and MPT-SNet (Mu, Shahzad, and Zhu 2025).

B.3 Experimental Details

We evaluate ERIS and the baseline methods on a server equipped with an Intel Xeon Gold 6346 CPU and two NVIDIA GeForce RTX 3090 GPUs (each with 24GB of memory), running Ubuntu 22.04.1 with CUDA 12.8 and PyTorch 2.7.0. To ensure rigor and reproducibility, all experiments are conducted using both GPUs with a fixed batch size of 64. For hyperparameter configuration, we primarily adhere to the settings of existing baseline methods. However, we also make necessary adjustments based on the characteristics of each dataset to optimize model performance. The models are trained for a total of 100 epochs. We utilize the Adam optimizer with an initial learning rate of $1e-4$. To facilitate better convergence, a StepLR learning rate scheduler is employed, decaying the current learning rate by a factor of

0.1 every 30 epochs. Additionally, the optimizer includes a weight decay of $1e-5$. Notably, the adversarial strength is dynamically adjusted throughout the training epochs to adapt to changes in the model’s training process. All experiments use a fixed random seed to guarantee the reproducibility of our results. For more details, please refer to our upcoming open-source repository.

B.4 Experimental Analysis

B.4.1 General Time Series Classification Results

In the main text, we have provided a thorough comparison of ERIS with related work in OOD and EBMs. To further establish the performance baseline of ERIS, we additionally compare it against a set of advanced general time series baselines. As shown in **Table 5**, ERIS achieves an overall average accuracy (Avg. ALL) of 75.47%, substantially outperforming all general time series baselines. Even when compared with the best-performing baseline, MPT-SNet (68.11%), ERIS demonstrates a performance gain of **more than 7%**, with a highly significant margin (p -value < 0.05). The advantage of ERIS is consistently and stably observed across all datasets, in stark contrast to the general-purpose baselines. Although these baselines adopt advanced architectures, they exhibit marked performance fluctuations across different target domains.

B.4.2 Mutual Information (MI) Analysis

Building upon correlation analysis, MI analysis offers a more comprehensive insight into inter-feature dependencies. Unlike feature correlation, which primarily captures linear relationships, MI can quantify various forms of dependencies, including nonlinear associations. Our observations from the MI matrices in **Figure 6** reveal the following:

- **Baseline (TSMixer):** The MI matrix of the baseline (Chen et al. 2023) exhibits pronounced off-diagonal intensities for several feature pairs (e.g., 0–2 and 4–6) alongside the expected diagonal dominance. Such patterns indicate that the dataset retains substantial redundancy and intricate cross-feature dependencies.
- **GILE:** Bright, dispersed yellow regions are observed throughout the MI matrix of GILE (Qian, Pan, and Miao 2021). While these patches confirm the preservation of strong nonlinear relationships, they also suggest that redundant or spurious dependencies have not been entirely suppressed.
- **ITSR:** Scattered yellow spots appear in the MI matrix of ITSR (Shi et al. 2024), yet the overall magnitude and density remain lower than those of both the baseline and GILE. Thus, ITSR partially attenuates cross-feature information, but nonlinear correlations are still incompletely removed.
- **ERIS (Ours):** By contrast, ERIS yields MI values that are markedly reduced away from the diagonal while preserving the high self-information expected along it. Redundant inter-feature information has therefore been substantially eliminated, resulting in a more compact representation that is expected to enhance generalization performance.

Datasets	Source Domain	Target Domain	ERIS (Ours)	TARNet (KDD'21)	PatchTST (ICLR'23)	TS-GAC (AAAI'25)	MPTNet (AAAI'25)
UCIHAR	1,2,3,4	0	94.70±1.20	73.43±5.55	94.31±0.31	93.20±0.81	94.51±0.38
	0,2,3,4	1	84.37±2.17	56.63±2.80	69.67±2.08	73.32±3.68	78.08±0.93
	0,1,3,4	2	95.05±1.00	92.03±3.28	94.30±0.39	93.61±1.49	93.03±1.27
	0,1,2,4	3	94.39±2.84	93.44±4.76	87.76±1.51	90.29±2.94	87.20±0.66
	0,1,2,3	4	97.42±0.98	77.68±2.83	93.58±3.57	94.77±0.60	96.30±1.23
Avg. Acc			93.19±4.91	78.64±14.26	87.92±9.82	89.04±8.42	89.82±6.81
UniMiB-SHAR	2,3,5	1	59.59±0.95	36.15±3.81	45.26±1.56	44.74±1.07	46.36±1.05
	1,3,5	2	49.34±0.83	34.17±7.60	42.89±1.63	42.99±0.78	47.14±2.29
	1,2,5	3	70.60±1.59	42.77±3.91	69.08±1.32	65.99±3.02	70.07±1.46
	1,2,3	5	41.41±0.81	33.50±2.21	39.94±0.63	39.47±0.66	41.28±1.09
Avg. Acc			55.23±11.30	36.65±5.80	49.29±11.95	48.30±10.78	51.21±11.50
EMG	1,2,3	0	73.59±1.84	50.59±2.92	48.24±1.04	48.88±0.48	43.86±0.54
	0,2,3	1	49.11±2.58	48.46±1.47	43.78±1.03	43.04±1.76	41.57±2.56
	0,1,3	2	65.12±6.20	44.77±2.06	40.00±1.62	41.51±1.46	51.52±1.58
	0,1,2	3	85.87±1.55	57.50±1.11	51.45±1.60	52.51±1.43	51.64±0.88
Avg. Acc			68.42±14.11	50.33±5.10	45.87±4.63	46.48±4.72	47.15±4.85
Opportunity	S2,S3,S4	S1	82.22±0.16	72.37±0.01	83.39±0.25	81.79±0.20	80.35±0.29
	S1,S3,S4	S2	81.10±0.28	71.98±0.01	81.01±0.62	80.92±0.15	79.25±0.44
	S1,S2,S4	S3	77.65±0.11	71.49±0.01	75.98±0.93	75.40±0.89	76.53±1.14
	S1,S2,S3	S4	82.25±0.13	73.40±0.00	81.37±0.55	81.77±0.32	79.27±1.01
Avg. Acc			80.81±1.94	72.31±0.73	80.59±2.90	79.97±2.77	78.85±1.63
Avg. ALL			75.47	60.61	67.17	67.31	68.11
<i>p</i> -value			-	≤ 1e-4	≤ 1e-4	≤ 1e-4	≤ 1e-4

Table 5: Overall comparison results of ERIS and general time series methods across four datasets (%). ‘Avg.’ is short for average, and the best performance is in **bold**. The *p*-value is obtained using the Wilcoxon signed-rank test; a value less than 0.05 indicates that the performance difference between ERIS and the compared method is statistically significant.

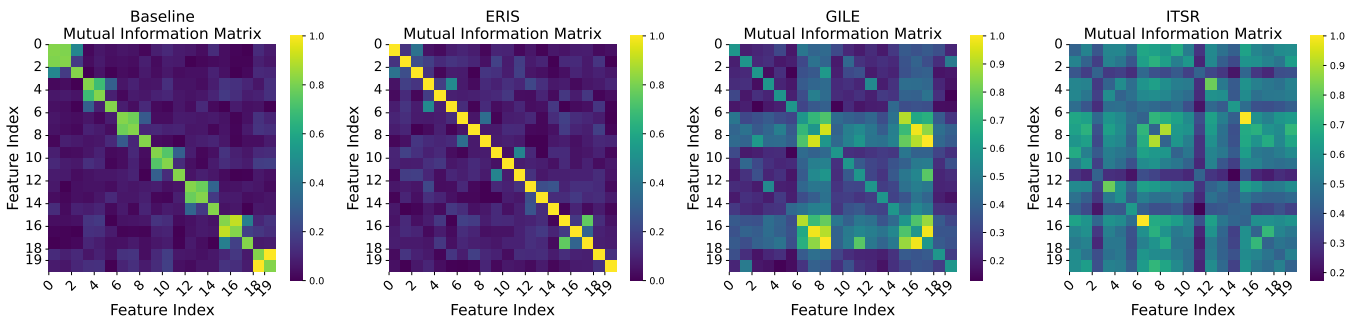


Figure 6: Visualizing orthogonal mutual information matrices. If two features are independent, their mutual information is zero. The higher the mutual information, the more information these two features share, meaning that knowing one feature reduces the uncertainty about the other.

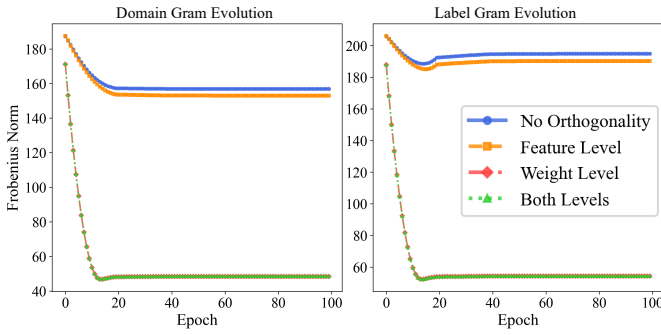


Figure 7: Impact of various orthogonality strategies on the Frobenius norm of model parameters during ERIS training on the UCIHAR dataset.

B.4.3 How do different orthogonality strategies have an impact on ERIS?

Theoretically, weight-level orthogonality strategy enforces structural independence between domain-specific and label-relevant feature subspaces by constraining the parameter space. We compare the evolution of the Frobenius norms under four different strategies (see **Figure 7**).

- **No Orthogonality:** Without an orthogonality constraint, the Frobenius norm of the weight matrices stabilizes at a high value. This lack of parameter control leads to overlapping subspaces for domain and label representations, resulting in the feature entanglement problem.
- **Feature-Level Orthogonality:** Applying a feature-level orthogonality strategy has a negligible effect on the Frobenius norm of the weight matrices. Its norm evolution curve is nearly identical to the baseline where no orthogonality is applied. This result validates our argument that feature-level orthogonality is a "per-instance" and local constraint. While it may decorrelate the feature representations for individual data points, it fails to impose global structural guidance on the underlying projection functions. Consequently, the parameter space itself can remain coupled, failing to provide a robust guarantee of feature separation for OOD samples.
- **Weight-Level Orthogonality (Ours):** In stark contrast to the aforementioned strategies, the weight-level orthogonality employed by ERIS demonstrates a significant effect. Applying this constraint causes the Frobenius norm of the weight matrices to decrease rapidly and substantially in the early stages of training, ultimately converging to a very low and stable level. This is achieved by directly optimizing the orthogonality penalty term $\mathcal{L}_{\text{ortho}}$. This loss term acts directly on the parameter matrices, continuously pushing the column spaces of \mathbf{W}_d and \mathbf{W}_l towards orthogonality. This global structural constraint enforces structural independence between the domain and label subspaces, fundamentally suppressing parameter redundancy and mitigating interference. This allows the model to learn clean and more invariant label-relevant representations.
- **Both-Level Orthogonality:** The experiment applying

both weight-level and feature-level constraints produced results nearly identical to using the weight-level strategy alone. This outcome confirms that weight-level orthogonality is the dominant regularization factor; adding a feature-level constraint provides no further benefit for parameter norm reduction, thus validating the efficiency of ERIS’s targeted approach.